Materials Today Bio 34 (2025) 102183

Contents lists available at ScienceDirect

Materials Today Bio

journal homepage: www.journals.elsevier.com/materials-today-bio

A tumor microenvironment-responsive Zr-MOF nanosystem for co-delivering siHIF-1α and triptolide enhances photodynamic therapy in esophageal cancer by amplifying ROS generation and reversing hypoxia

Wenhan Liu [a,1], Can Sun [b,1], Yuhang Dai [a], Huaiyong Wang [a], Milad Ashrafizadeh [c], João Conde [d,*], Liyu Yang [e,**], Wei He [a,***]

[a] Department of Thoracic Surgery, The Shengjing Hospital of China Medical University, Shenyang, Liaoning, 110004, PR China
[b] Department of Clinical Nutrition, The Shengjing Hospital of China Medical University, Shenyang, Liaoning, 110004, PR China
[c] Department of Radiation Oncology and Shandong Provincial Key Laboratory of Radiation Oncology, Shandong Cancer Hospital and Institute, Shandong First Medical University and Shandong Academy of Medical Sciences, Jinan, Shandong, 250117, PR China
[d] Comprehensive Health Research Centre (CHRC), NOVA Medical School, Faculdade de Ciências Médicas, NMS|FCM, Universidade NOVA de Lisboa, Lisboa, Portugal
[e] Department of Orthopedics, The Shengjing Hospital of China Medical University, Shenyang, Liaoning, 110004, PR China

ARTICLE INFO

Keywords:
Esophageal cancer
Metal-organic framework
Photodynamic therapy
Drug and gene delivery
Reactive oxygen species

ABSTRACT

In addition to early diagnosis and on-time treatment, the adoption of new therapeutic strategies is of great significance for improving the clinical outcomes of patients with esophageal cancer. Although emerging therapies such as photothermal and photodynamic therapy (PDT) can precisely eliminate cancer cells and are alternative strategies to conventional treatments, hypoxia status of solid tumors have hindered their application. In recent years, nanoplatforms have been developed to address these limitations and improve the efficacy and safety of treatments. In addition, triptolide (TPL) and HIF-1α silencing may have potential value in cancer treatment by regulating oxidative stress. Inspired by these findings, we designed a cancer cell membrane-camouflaged porphyrin (photosensitizer) metal-organic framework (Zr-MOF@CM) for the co-delivery of TPL and HIF-1α small interfering RNA (siRNA) into tumor cells and tissues. The nanoparticles (TPL/siHIF-1α@Zr-MOF@CM) achieved targeted drug/gene/PDT synergistic therapy for esophageal cancer. This portable "all-in-one" drug delivery system exhibited good biocompatibility, sensitive pH-dependent drug release, and effective phagocytosis by esophageal cancer Kyse-30 cells. In addition, the nanoparticles produced large amounts of ROS and released drugs under near-infrared light (660 nm) irradiation, which significantly increased the apoptosis of esophageal cancer cells. Meanwhile, TPL and siHIF-1α released from the nanoparticles alleviated the hypoxic condition, further improving the PDT effect. In vivo experiments confirmed that TPL/siHIF-1α@Zr-MOF@CM maintained a long circulation time in tumor-bearing mice, specifically targeted the tumor site, and played a synergistic role with PDT to effectively reduce tumor growth. Importantly, TPL/siHIF-1α@Zr-MOF@CM exhibited a favorable biosafety profile in vitro and in vivo. This nanosystem is suitable for enhancing oxidative damage at tumor sites and is instructive for future design of PDT-dependent nanoplatforms.

1. Introduction

As a global health problem, the morbidity and mortality rates of esophageal cancer rank 7th and 6th among all types of cancer, respectively [1]. Despite advances in the new treatment modalities, the prognosis for esophageal cancer remains poor, requiring novel strategies in improving survival of patients. Moreover, a study has demonstrated that it is estimated that by 2040, up to 957,000 cases are diagnosed with 880,000 deaths [2]. This is mainly because early esophageal cancer usually has no obvious clinical symptoms, and most cases are diagnosed

* Corresponding author.
** Corresponding author.
*** Corresponding author.
E-mail addresses: joao.conde@nms.unl.pt (J. Conde), yanglycmu@126.com (L. Yang), 13889858921@163.com (W. He).
[1] These authors contributed equally to this work.

https://doi.org/10.1016/j.mtbio.2025.102183
Received 29 March 2025; Received in revised form 26 July 2025; Accepted 9 August 2025
Available online 13 August 2025

in the advanced stages when treatment options are limited. As a result, more advances should be performed in the treatment and diagnosis of esophageal cancer, such as application of immune checkpoint inhibitors and minimally-invasive strategies [3]. Currently, the treatment of esophageal cancer mainly involves surgical resection, chemotherapy, radiotherapy, and appropriate adjuvant immunotherapy for residual lesions [4]. Although surgical treatment can improve patient outcomes, it is accompanied by the risk of an anastomotic fistula, which triggers serious complications such as pneumonia and sepsis [5]. In addition, chemotherapy may damage healthy cells while limiting tumor growth, thereby leading to non-specific cytotoxicity. Notably, the drug release process is difficult to control, and targeted drugs do not always reach the cells within the tumor. Therefore, developing specific therapies that actively target cancer cells is necessary to minimize the off-target effects and systemic toxicity.

The progresses in nanobiotechnology have been beneficial in improving and addressing this problem. A wide variety of nanocarriers have been developed for drug delivery, aiming to reduce poor drug distribution and systemic adverse effects of the drugs. Among them, nanometer-sized metal-organic frameworks (MOFs) have become ideal carriers for the controlled drug release owing to their porous internal structure and easily adjustable pore size, which provide good loading sites and protection for small molecular drugs [6]. Moreover, compared to the conventional porous materials, MOFs can introduce specific chemical groups on its organic ligands through post-synthetic modification, thereby endowing MOFs with new chemical properties or biological activities [7]. MOF materials can also be used in combination with various modalities such as chemotherapy, radiotherapy, and photodynamic therapy (PDT), and have received extensive attention in the medical field (cancer treatment and wound healing) [8–10]. In particular, the zirconium (Zr)-based porphyrin MOF (Zr-MOF, also known as PCN-224) not only serve as nanocarriers for drug loading, but are also good photosensitizers in their own right with deep penetration properties. This unique characteristic makes it beneficial for PDT. Therefore, there has been a special attention to the application of Zr-MOFs in PDT for cancer therapy [11,12]. PDT is a new type of treatment method that combines three essential substances: photosensitizer, oxygen, and light. When exposed to laser light at a specific wavelength, the photosensitizer reacts with molecular oxygen to produce toxic reactive oxygen species (ROS), ultimately leading to cell death [13]. This minimally invasive, highly curative, and low side-effect advantages of PDT make it an alternative method to conventional cancer treatment. Therefore, different studies have focused on the application of PDT in cancer therapy [14–16]. Despite the remarkable success of PDT in improving the survival of patients with esophageal cancer, the hypoxic environment within the tumor remains a significant obstacle to its widespread clinical application. Most solid tumors exist in a hypoxic state due to the abnormal proliferation and dysfunctional angiogenesis of wild heterogeneous tumor cells, which significantly reduces the therapeutic efficiency of PDT. Therefore, hypoxia has been considered in process of PDT and nanoparticles are suggested to improve hypoxia and increase potential of PDT [17,18]. Meanwhile, oxygen depletion during PDT process further exacerbates tumor hypoxia, and then synergistically produces severe side effects after PDT. To overcome the limitations of PDT, efforts are being made to explore new therapeutic strategies to circumvent tumor hypoxia [19]. Notably, tumor cells acquire multiple adaptive capabilities in the hypoxic microenvironment, such as inducing the binding HIF-1α to hypoxia-responsive elements in the VMP1 promoter, triggering VMP1-associated autophagy to increase tumor cell survival, thus promoting tumor cell resistance to PDT [20]. Hence, inhibition of HIF-1α expression is considered to be sensible and effective approach to enhance the anti-tumor activity of PDT [21,22]. Small interfering RNA (siRNA) can selectively inhibit the expression of pathogenic genes and has promising application in the treatment of various diseases such as cancer [23]. However, HIF-1α siRNA has been rarely evaluated in esophageal cancer. Moreover, HIF-1α may have its own issues including off-targets, lack of precise accumulation in tumor tissue and low circulation in blood stream along with degradation by RNA enzymes. Currently, the development of nanomaterials can effectively encapsulate nucleic acids and protect genetic drugs from degradation [24,25]. Hence, the present study focused to enhance the bioavailability of siHIF-1α by delivering it through the nanoplatform Zr-MOF.

Although the fact that PDT can locally treat primary tumors, PDT alone does not completely treat metastatic cancer and recurrence. This is because of the malignant and progressive nature of metastatic and recurrent tumors, limiting the efficacy of therapeutics. Numerous research efforts have been devoted to combining PDT with chemotherapy to achieve synergistic anti-tumor effects, and this approach has made significant progress [26–28]. The natural extract triptolide (TPL) has a wide range of anti-tumor pharmacological effects, including induction of ROS generation and apoptosis [29]. Enhancement of ROS generation is also a key strategy to improve the efficacy of PDT. The nanoparticles developed by Yang et al. achieved simultaneous local ROS generation and hypoxia reversal, effectively enhanced PDT, and exerted strong anti-tumor effect and anti-recurrence ability in pancreatic cancer [30]. Although TPL has been suggested as a potent anti-cancer agent and it can improve the sensitivity of tumor cells to chemotherapy, there are a number of issues with TPL including poor solubility and pharmacokinetic profile. Therefore, nanoparticles have been suggested for the delivery of TPL to improve its therapeutic index. Notably, understanding the efficacy of TPL and PDT combination in esophageal cancer therapy requires further evaluation. More importantly, to address the limited biocompatibility and targeting of nanomedicines, it has been suggested to coat the surface of nanoparticles with different types of cell membranes to develop bionic cell membrane camouflaged nanoparticles [31]. Among several commonly used cell membranes, cancer cell membrane is particularly remarkable due to diverse surface molecular features such as adhesion molecules. It exhibits a range of cancer cell mimetic properties that can evade immune surveillance and target homologous cells [32,33]. Thus, cancer cell membrane-coated nanoparticle may be a promising tool for cancer therapy.

Herein, we designed cancer cell membrane-encapsulated materials Zr-MOF@CM with the introduction of TPL and siHIF-1α, to achieve synergistic anti-tumor effects of PDT, chemotherapy, and gene-targeted therapy. This nanomedicine exhibits outstanding therapeutic effects both in vivo and in vitro. Briefly, when TPL/siHIF-1α@Zr-MOF@CM reached the tumor site, 660 nm light irradiation activated the photosensitized H_2TCPP in Zr-MOF@CM, and then stimulated the production of ROS, thereby destroying cancer cells. Meanwhile, TPL and siHIF-1α released from the nanoparticles alleviated the hypoxic condition, further improving the PDT effect. Ultimately, these nanoparticles were excreted through the kidneys, without causing actual toxicity. Overall, TPL/siHIF-1α@Zr-MOF@CM exhibits excellent PDT performance and hypoxia adaptability, making it suitable for the treatment of esophageal cancer. The long-term efficacy and clinical translation of this system are still being explored.

2. Materials and methods

2.1. Materials and reagents

$ZrOCl_2{\cdot}8H_2O$ (S24323), benzoic acid (T92835), and N,N-dimethylformamide (DMF, Y46524) were obtained from Shanghai Yuanye Bio-Technology Co., Ltd. (Shanghai, China). H_2TCPP (P816654) was purchased from Shanghai Macklin Biochemical Co., Ltd. (Shanghai, China). TPL (ST8290), acetonitrile (IO0160), trypsin (T1300), and TBST (T1085) were obtained from Beijing Solarbio Science & Technology Co., Ltd. (Beijing, China). DEPC-water (R0021), PBS (C0221A), Tris-HCl (ST789), $MgCl_2$ (R0058), TMB (ST746), SDS-PAGE buffer (P0015A), DAPI staining (C1005), H&E staining (C0105S), Coomassie brilliant blue staining (P0017), DMSO (ST038), ROS detection kit (S0033S), CCK-8 reagent (C0037), TUNEL staining (C1091), Annexin V-FITC apoptosis

detection kit (C1062S) was purchased from Beyotime Biotechnology (Shanghai, China). FBS (#26-500-FBS) was obtained from EPHRAIM (Xiamen, China). FAM (AM4620) was from ThermoFisher (Massachusetts, USA). Cy5 (HY-D0821) and DPBF (HY-W011664) were purchased from MCE (Shanghai, China). Live/dead cell double staining kit (B-CHK103-500T) was obtained from Biogradetech (California, USA). FastKing gDNA Dispelling RT SuperMix (KR118-02) was derived from TIANGEN (Beijing, China). The SYBR Green PCR kit (A4004M) was derived from Lifeint (Xiamen, China). ECL chemiluminescent solution (P1000) was obtained from APPLYGEN (Beijing, China). FITC anti-mouse/human CD44 (#103006) and CD90 (#328107) were purchased from Biolegend (California, USA). FITC fluorescent Anti -EGFR antibody (ab11400) and GAPDH antibody (ab181602) were acquired from Abcam (Shanghai, China). Ki67 antibody (AF0198) was purchased from Affinity (Jiangsu, China).

2.2. Synthesis of Zr-based MOF

The Zr-MOF was synthesized using a solvothermal method, as previously described [34]. Benzoic acid (2.8 mg), $ZrOCl_2{\cdot}8H_2O$ (300 mg), and H_2TCPP (100 mg) were dissolved in DMF (100 mL), followed by stirring in a nitrogen atmosphere at 90 °C for 5 h. After cooling to room temperature, the MOF precipitates were obtained by centrifugation at 10000×*g*, and then washed with DMF for three times. The collected MOF nanoparticles were stored in DMF at 4 °C for later use.

2.3. Synthesis of TPL/siHIF-1α@Zr-MOF

TPL (80 mg, 98 % purity) was mixed with acetonitrile (2 mL) under sonication beforehand, and then Zr-MOF (20 mg) was added. The samples were vigorously stirred with a magnetic stirrer at 500 rpm for 24 h at room temperature, followed by centrifugation for 10 min at 10000×*g* to collect the TPL@Zr-MOF. Before further application, the TPL@Zr-MOF was washed with acetonitrile for three times, and dried under vacuum at room temperature overnight. To prepare nanoparticles loaded with siHIF-1α, we dropped siHIF-1α into TPL@Zr-MOF (dissolved in DEPC water) and maintained the mass ratio of nanoparticles to siRNA at 5:1. This ratio was determined based on the results of siRNA encapsulation rate. In brief, the mixtures of siHIF-1α (FAM-labeled) and Zr-MOF material with different ratios (1:1, 1:5, 1:10, 1:15) were centrifuged at 15,000 g for 15 min and the supernatant was collected. The absorbance was measured at 490 nm using a spectrophotometer (NanoDrop™3300, ThermoFischer Scientific) to reflect the content of FAM-siRNA in the supernatant. It was then compared with the total dosage of FAM-siHIF-1α during the encapsulation process to evaluate the encapsulation rate, with the following equation: Encapsulation efficiency (%) = $(M_T\text{-}M_F)/M_T \times 100$ %. Where M_T and M_F indicate the total siRNA content and the amount of siRNA in the supernatant, respectively. After that, the mixed solution was incubated at a shaking speed of 100 rpm for 30 min and then centrifuged at 13000 rpm for 15 min. Finally, the samples were washed three times with DEPC water to remove free siHIF-1α and the precipitate was collected to obtain TPL/siHIF-1α@Zr-MOF. The sequences of siHIF-1α were designed by Designer of Small Interfering RNA website (http://biodev.extra.cea.fr/DSIR/DSIR.html), with sense strand, 5′-UUCAGAUUCUUUACUUCGCCG-3′ and antisense strand, 5′-GCGAAGUAAAGAAUCUGAAGU-3'.

2.4. Extraction of cell membrane from esophageal cancer

Collected Kyse-30 cells were washed with PBS and re-suspended in a hypotonic lysate buffer (10 mM Tris-HCl and 2 mM $MgCl_2$) at pH 7.5, followed by performing mechanical destruction for 60 s to obtain cell homogenates. The cell samples were centrifuged at 3200×*g* for 5 min (4 °C), and the obtained supernatant was continued to be centrifuged under the same condition to collect the supernatant containing crude cell membrane (CM) extracts. Afterwards, the supernatant was centrifuged at 100000×*g* for 30 min (4 °C) and the collected precipitate was suspended in the buffer (10 mM Tris-HCl and 10 mM EDTA, pH 7.4), and then centrifuged again at 100000×*g* for 30 min. After resuspending the precipitate with PBS, the solution was extruded using a 400 nm polycarbonate membrane to obtain CM fragments. The CM samples were freeze-dried and stored at −80 °C.

2.5. Preparation of TPL/siHIF-1α@Zr-MOF@CM complex

The above esophageal cancer CM was re-suspended in PBS buffer and mixed with TPL/siHIF-1α@Zr-MOF. Then, the mixture was treated with ultrasound (40 kHz) for 3 min and physically extruded once through a smaller polycarbonate film (200 nm). Finally, the free CM was removed by centrifugation at 5000×*g* for 30 min, and the collected product was CM-coated TPL/siHIF-1α@Zr-MOF (denoted as TPL/siHIF-1α@Zr-MOF@CM). Besides, Zr-MOF@CM, TPL@Zr-MOF@CM, and siHIF-1α@Zr-MOF@CM were all prepared by the above methods expect for the use of drugs alone or without.

2.6. Identification of CM-associated markers

We first confirmed the presence of cancer cell membrane-associated proteins in the nanoparticles using Coomassie blue staining. Protein samples of Kyse-30 CM, TPL/siHIF-1α@Zr-MOF, and TPL/siHIF-1α@Zr-MOF@CM were obtained by RIPA lysis buffer and the protein content was determined using BCA protein assay kit. Protein profiles were verified by 10 % SDS-PAGE, following by staining with Coomassie blue for 1 h. After removing the blue background by washing with ultrapure water, the gel was imaged with a digital camera.

Specific protein markers of CM were further detected by flow cytometry. Briefly, Kyse-30 cells, Kyse-30 CM, and TPL/siHIF-1α@Zr-MOF@CM nanoparticle were resuspended with 200 μL of PBS. Then, CD44, CD90, and EGFR antibodies were added to the samples and incubated for 30 min at room temperature. After centrifugation, the precipitates were resuspended with PBS, followed by application of flow cytometry (No. DR-3518G, Wuxi Hiwell Diatek Instruments Co., Ltd, Jiangsu, China) to detect the fluorescence intensity of samples.

2.7. Physicochemical characterization of nanoparticles

The physicochemical properties of the nanoparticles were characterized through a series of experiments. Specifically, 100 μL of nanoparticle solution was mixed with 1.9 mL of deionized water; after ultrasound for 5 min, the particle size and zeta potential of the nanoparticles were measured by SYNC (Microtrac, Shanghai, China) and BeNano 180 Zeta Pro (Dandong Baxter Instrument Co., LTD, Liaoning, China), respectively. The structures of the compounds in the nanoparticles were qualitatively analyzed by UV–Vis spectroscopic detection, with the help of dual-beam spectrophotometer U-2910 (Thermo, MA, USA). In addition, the fluorescence properties of MOF in the different nanoparticles were determined at an excitation wavelength of 380 nm. Besides, the 2 mg nanoparticle powder was subjected to KBr compression, and then the molecular structure and functional groups of the samples were detected using Fourier transform infrared spectrometer (Spectrum 1000, Perkin-Elmer, MA, USA). The parameters were as follows: wave number in the range of 400 cm^{-1}∼4000 cm^{-1}, resolution of 4 cm^{-1}/s, and scanning time of 16 s. XRD analysis was performed using a polycrystalline X-ray diffractometer (D8 AdvanceX, Bruker, MA, USA) to determine the crystal structure in the nanoparticle samples. We also assessed the major elements (carbon [C], nitrogen [N], oxygen [O], zirconium [Zr]) of the nanomaterials by energy dispersive X-ray spectroscopy. Moreover, based on the nitrogen adsorption-desorption isotherms, the pore size structure and surface properties of the nanomarterials were analyzed on the Autosorb-iQ3 instrument. Following, the morphologies of Zr-MOF, Zr-MOF@CM, and TPL/siHIF-

1α@Zr-MOF@CM were characterized by transmission electron microscopy (TEM, HT7800, HITACHI, Tokyo, Japan).

2.8. Assessment of drug loading rate and drug release

The concentration of TPL in TPL/siHIF-1α@Zr-MOF@CM was evaluated by UV–Vis spectrophotometry. First, 1 mg of TPL was dissolved in 1 mL of DMSO, and the TPL standard curve was prepared according to the concentration gradients (0, 31.25, 62.5, 125, 250, and 500 μg/mL). Subsequently, TPL/siHIF-1α@Zr-MOF@CM powder was prepared into 5 mg/mL aqueous solution and centrifuged at 12000 r/min for 10 min. After diluting the collected supernatant, the absorption value was measured at 220 nm and the TPL concentration in the supernatant was calculated based on the standard curve. The drug-loading efficiency (DLE) was calculated using the following formula: DLE (%) = $(W_{total}-W_{sup})/W_{total} \times 100$ %. Here, W_{total} and W_{sup} represent the masses of TPL in the nanoparticle and supernatant, respectively.

To evaluate the release characteristics of the drugs (TPL and siHIF-1α) in slightly acidic and physiological environments, TPL/siHIF-1α@Zr-MOF@CM was suspended in a dialysis bag containing pH 5.5 or 7.4 PBS (2 mL). The sealed dialysis bags were placed in bottles containing 20 mL of PBS buffer at 37 °C with continuous agitation in the dark for 24 h. The solution (10 μL) in the dialysis bag was collected at the indicated time points, and drug release was detected using UV spectrophotometry (TPL) or fluorescence spectrophotometry (FAM-labeled siHIF-1α). The released drug was defined as the percentage of drug in PBS to the total drug encapsulated in TPL/siHIF-1α@Zr-MOF@CM particles.

2.9. Evaluation of nanoparticle stability

We also utilized dynamic light scattering (DLS) to detect the size changes of TPL/siHIF-1α@Zr-MOF@CM nanoparticles in different culture media to reflect their stability. Briefly, TPL/siHIF-1α@Zr-MOF@CM powder was dissolved in DMSO, and the particle size in PBS or 10 % FBS media was examined at specific time points.

2.10. Detection of •OH releasing

To assess the ability of •OH generation, UV spectrophotometry was used to evaluate the absorbance values of the nanoparticles at different time points under 660 nm laser irradiation. In brief, 5 μL of TPL/siHIF-1α @Zr-MOF@CM was added to a centrifuge tube, and 2.5 mL of deionized water was added. Then, 10 μL of H_2O_2 (mass concentration of 5 %) and 25 μL of TMB were added to the mixture. After the solution changed color, the intensity of the absorption peak at 455 nm was measured to reflect the formation of •OH.

2.11. Detection of singlet oxygen ($^1O_2$) generation

The formation of $^1O_2$ in nanoparticles was detected using a DPBF kit. First, 15 g of DPBF was dissolved in 1 mL of DMSO and then mixed with Zr-MOF or TPL/siHIF-1α @Zr-MOF@CM nanoparticles (dispersed in DMSO). The mixture was irradiated with a 660 nm laser (0.5 W/cm^2) for 300 s. The absorbance of DPBF at 410 nm was recorded using a UV spectrophotometer.

2.12. Cell lines

The human esophageal squamous cell carcinoma cell line Kyse-30 was obtained from Wuhan Pricella Biotechnology Co., Ltd. (CL-0577) and cultured according to the manufacturer's guidelines (RPMI-1640 medium containing 10 % FBS and 1 % penicillin-streptomycin). Cells were maintained at 37 °C in humidified air with 5 % CO_2 and passaged when growth reached 80 %.

2.13. In vitro cytotoxicity assay

The in vitro cytotoxicity of the nanomaterials was evaluated using the CCK-8 method. Kyse-30 cells were inoculated into 96-well plates at a density of 2000 cells/well. After overnight culture, the cells were incubated with different concentrations of Zr-MOF or Zr-MOF@CM for 24 h, and then CCK-8 solution was added and incubated for 2 h. The absorbance of the samples was measured at 450 nm. In addition, we evaluated the photo-responsive characteristics of the nanoparticles. Briefly, Kyse-30 cells treated with Zr-MOF@CM or TPL/siHIF-1α@Zr-MOF@CM were irradiated with 660 nm lasers of different powers (0, 0.3, 0.6, and 1 J/cm^2) for 24 h, and cell viability was detected using the CCK-8 method.

2.14. Cellular uptake assay

To assess the cellular uptake of nanoparticles, we performed flow cytometry and confocal laser scanning microscopy (CLSM) assays. Kyse-30 cells were inoculated into 6-well plates at a density of 5×10^5 cells/well. After overnight incubation, cells were treated with TPL/siHIF-1α@Zr-MOF or TPL/siHIF-1α@Zr-MOF@CM for 0, 2, 4, and 6 h, respectively. The fluorescence intensity was then measured using flow cytometry. For the CLSM assay, cells in the different treatment groups were washed three times with PBS and fixed with 70 % ethanol for 2 h. Subsequently, DAPI staining was performed for 15 min and the cellular uptake was observed under CLSM (TCS SP8, Leica, Wetzlar, Germany).

2.15. Hemolysis test

Erythrocytes were extracted from whole blood of BALB/c nude mice and washed with cold sterile saline until the supernatant was clear. Erythrocyte suspensions (100 μL) were added to PBS buffer (negative group), deionized water (positive group), or TPL/siHIF-1α@Zr-MOF@CM dispersion at concentrations of 6.25 μg/mL, 12.5 μg/mL, 25 μg/mL, 50 μg/mL, 100 μg/mL, or 200 μg/mL. After 12 h, the mixtures were centrifuged, and the absorbance of the supernatants of each group was measured at 541 nm. The hemolysis rate was calculated using the formula: hemolysis rate = $[(A_{samples} - A_{PBS})/(A_{water} - A_{PBS}) \times 100$ %.

2.16. Cell viability and apoptosis assays

Kyse-30 cells were inoculated in 96-well plates (2000 cells/well) and cultured overnight at 37 °C. Cells were then treated with Zr-MOF@CM, TPL@Zr-MOF@CM, siHIF-1α@Zr-MOF@CM, or TPL/siHIF-1α@Zr-MOF@CM (50 μg/mL) for 24 h. We also explored the therapeutic effect of PDT with nanoparticles, and set up additional laser treatment groups. After treatment with nanoparticles for 24 h, cells were irradiated with a 660 nm laser for 5 min. Following, CCK-8 was utilized to detect cell proliferation after incubation for 24 h. In addition, apoptosis of Kyse-30 cells was detected with Annexin V-FITC/PI assay kit. Briefly, cells in each group were digested with 0.25 % trypsin and washed twice with cold PBS buffer. After centrifugation for 5 min (1500 rpm), cells were stained with Annexin V-FITC and PI solutions, according to the manufacturer's protocol. Afterwards, cells were assayed by flow cytometry and the data were analyzed using CELL Quest software.

2.17. Live/dead cell detection

The survival state of cells was tested using Calcein AM/PI kit. Kyse-30 cells were incubated with different nanoparticles in the presence or absence of laser for 24 h. Subsequently, the cells were collected for digestion. After washing twice with PBS, cells were incubated with Calcein AM and PI staining reagents in the dark for 15 min. Next, dead cells (red fluorescence) and live cells (green fluorescence) were observed under a fluorescence microscope.

2.18. Intracellular ROS detection

The level of intracellular ROS production was assayed using the ROS commercial kit. Kyse-30 cells were treated with different nanoparticles, including Zr-MOF@CM and TPL/siHIF-1α@Zr-MOF@CM, in 96-well plates for 24 h. Then, the ROS assay was performed after laser irradiation at 660 nm for 5 min. After PBS washing, 10 μM DCFH-DA was added to the cells and incubated in 37 °C incubator for 20 min. In addition, cell nuclei were stained with DAPI. The fluorescence intensity of the cells was determined by an enzyme labeling instrument with the excitation and emission peaks at 488 nm and 525 nm, respectively. Meanwhile, ROS level was quantified by FlowJo software.

2.19. Evaluation of HIF-1α protein level via western blot experiment

To evaluate the knockdown effect of the nanomaterials, the level of HIF-1α in the cells were measured using western blot. Specifically, Kyse-30 cells were cultured in 6-well plates (2×10^5 cells/well) and treated with free siNC, free siHIF-1α, or TPL/siHIF-1α@Zr-MOF@CM for 24 h. Meanwhile, free siHIF-1α and TPL/siHIF-1α@Zr-MOF@CM-treated cells were also subjected to corresponding laser irradiation groups (660 nm laser for 5 min). Then, protein samples of cells in each group were collected and quantified by BCA method. After electrophoretic separation and membrane transfer, protein samples were incubated with primary antibodies against HIF-1α (1 : 1000) or GAPDH (internal reference, 1 : 10000) overnight at 4 °C. After washing with TBST buffer, the protein samples were reacted with secondary antibody for 1 h at room temperature. ECL luminescence kit was adopted for imaging, followed by quantification of protein signals using a chemiluminescence imager and Image Lab.

2.20. Quantitative RT-PCR (qRT-PCR)

Using HIF-1α as target gene, qRT-PCR was employed to explore the knockdown efficiency and stability of siRNA. Kyse-30 cells were cultured in 6-well plates (2×10^5 cells/well), treated with nanoparticles for 48 h, and cells were collected. We also collected the treated cells after three consecutive passages. Cells were washed with PBS three times and lysed with Trizol to extract total RNA. cDNA was synthesized for each sample using the FastKing kit. Then, qRT-PCR reactions were performed to quantify the mRNA expression of HIF-1α and GAPDH (housekeeping gene), with the help of a SYBR Green PCR kit and a real-time fluorescent quantitative PCR system. All primer sequences were: HIF-1α (121 bp), forward: 5′-GGCGCGAACGACAAGAAAAA-3′, reverse: 5′-GTGGCAACTGATGAGCAAGC-3’; GAPDH (236 bp), forward: 5′-AGCTTCAGCCCCAGGAAATC-3′, reverse: 5′-GACATACTGCTGGGCCAGTT-3’. Relative gene expression was quantified by $2^{-\Delta\Delta Ct}$.

2.21. Animal models

The 4-week-old male BALB/c nude mice were purchased from the Experimental Animal Center of Yangzhou University. All mice were acclimated for one week before formal experiments. Animal experiments were performed following the protocol approved by the Ethics Committee of Yangzhou University, with license No. 202407034. Kyse-30 cells (3×10^6) were injected subcutaneously into the right axilla of each mouse to establish the tumor model. When the tumor volume reached ~100 mm^3, the mice were subjected to subsequent treatment. All animal experiments were approved by the Institutional Animal Care and Use Committee of Yangzhou University (Ethics No. 202407034).

2.22. In vivo biodistribution

The in vivo biodistribution of TPL/siHIF-1α@Zr-MOF or TPL/siHIF-1α@Zr-MOF@CM was observed by an imaging system. TPL/siHIF-1α@Zr-MOF or TPL/siHIF-1α@Zr-MOF@CM nanoparticles (20 mg/kg; labeled with Cy5) suspended in PBS were injected into Kyse-30 tumor-bearing mice by tail vein injection. In vivo fluorescence images of mice at different time points (2, 4, 6, 8, 12, 24 h) were captured using an in vivo visible light imaging system (FLIR E4, Pumeng technology, Shanghai, China), with Cy5 fluorescence channel (640 nm excitation and 680 nm emission). Besides, the mice were executed 48 h after drug administration and the major organs (heart, liver, spleen, lung, kidney, and tumor) were separated. The metabolism of nanoparticles in various organs was observed by a fluorescence imaging system.

2.23. In vivo antitumor efficiency evaluation

Kyse-30 tumor bearing mice were randomly divided into the following four groups (n = 6): 1) control, 2) Zr-MOF@CM + laser, 3) TPL/siHIF-1α@Zr-MOF@CM, and 4) TPL/siHIF-1α@Zr-MOF@CM + laser. Mice in the treatment groups were injected with the corresponding nanoparticles via tail vein every 2 days during the treatment for 14 d. For the group requiring laser irradiation, mice were additionally irradiated with a 660 nm laser for 15 min after administration of drugs for 6 h. Tumor volume and body weight of the mice were examined daily during treatment. Tumor volume was calculated using length × $weight^2/2$.

2.24. Histology and immunohistochemical analysis

At the end of the anti-tumor research (after two weeks), the tumor and major organs were collected, followed by preparation of tissue sections via fixing with 4 % paraformaldehyde and embedding in paraffin. To evaluate the efficacy of treatment, TUNEL and Ki67 immunohistochemical staining was performed on tumor sections. Proteins from tumor samples were also extracted for western blot analysis to detect the expression level of HIF-1α. Moreover, H&E staining of major organs was conducted to investigate the biosafety of nanoparticles or combination therapy.

2.25. Statistics

Data were presented as mean ± SD and statistically analyzed by GraphPad (version 7.0). Differences between groups were compared by *t*-test (two groups) or ANOVA test (multiple groups) and significance was determined by the following thresholds: *P < 0.05 and **P < 0.01.

3. Results

3.1. Morphology and characterization of TPL/siHIF-1α@Zr-MOF@CM

In our design, the core of the nanomaterials consisted of a Zr-MOF organic framework and a cancer cell membrane (CM) for coating. Moreover, the anticancer drug TPL and small nucleic acid drug siHIF-1α were loaded into the nanoplatform, and the nanomedicine TPL/siHIF-1α@Zr-MOF@CM was constructed by ultrasonic and physical extrusion. We first optimized the delivery ratio of siHIF-1α and Zr-MOF. Fluorescence analysis revealed that the highest encapsulation rate of siRNA was achieved when the weight ratio of siHIF-1α: Zr-MOF was 1:5, about 37 % (Fig. 1A). Therefore, in the following experiments, 1:5 of siHIF-1α: Zr-MOF was selected as the final ratio for nanoparticle preparation. Subsequently, the morphology of the nanoparticles was characterized. TEM images showed that the prepared Zr-MOF possessed spherical structure with the smooth surface. After coating the Kyse-30 cell membrane, the resulting nanoparticle TPL/siHIF-1α@Zr-MOF@CM exhibited a distinctive core-shell structure (Fig. 1B). The particle size of Zr-MOF was 180.2 nm; after CM encapsulation and drug loading, the diameter of TPL/siHIF-1α@Zr-MOF@CM was increased to 198.8 nm (Fig. 1C). Element mapping analysis detected a uniform distribution of Zr, N, C, and O simultaneously in TPL/siHIF-1α@Zr-MOF@CM (Fig. 1D). In addition, zeta potential of Zr-MOF was 5.7 mV. After drug loading, the

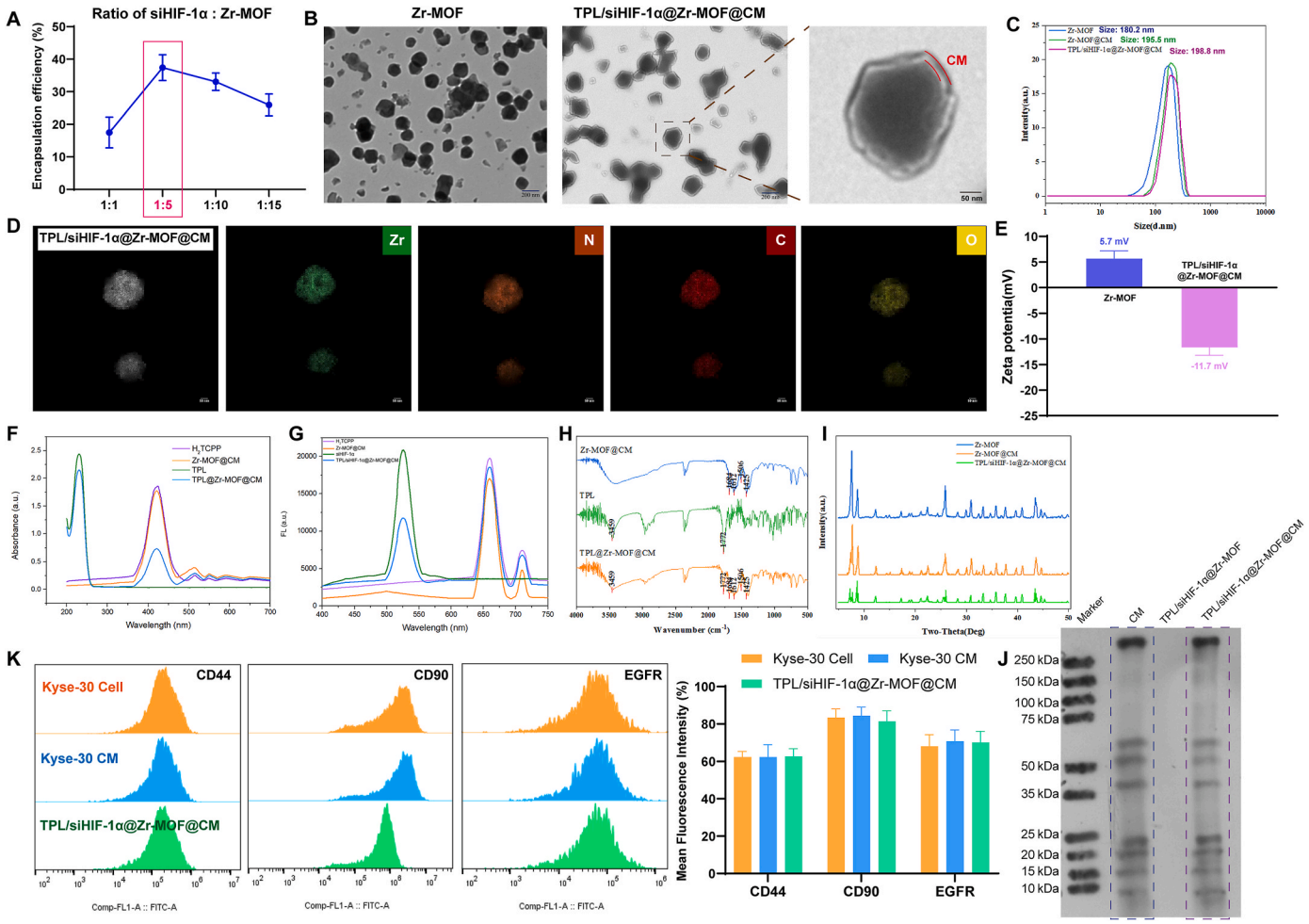

Fig. 1. Characterization of TPL/siHIF-1α@Zr-MOF@CM. A) Fluorescence analysis identified the optimal weight ratio of siHIF-1α to Zr-MOF. B) TEM (scale bars: 200 nm) and amplified TEM images (scale bars: 100 nm) of Zr-MOF and TPL/siHIF-1α@Zr-MOF@CM. C) The particle sizes of Zr-MOF, Zr-MOF@CM, and TPL/siHIF-1α@Zr-MOF@CM. D) Element mapping images (Zr, N, C, and O elements; scale bar, 50 nm). E) The zeta potential of Zr-MOF, Zr-MOF@CM, and TPL/siHIF-1α@Zr-MOF@CM. F) UV–vis absorption spectra of Zr-MOF@CM, TPL, and TPL@Zr-MOF@CM dissolved in DMSO. G) Fluorescence spectrum of Zr-MOF@CM, siHIF-1α, and TPL/siHIF-1α@Zr-MOF@CM (siRNA labeled with FAM). H) FTIR spectrum of Zr-MOF@CM, TPL, and TPL@Zr-MOF@CM. I) XRD patterns to characterize crystal states in Zr-MOF, Zr-MOF@CM, and TPL/siHIF-1α@Zr-MOF@CM. J) SDS-PAGE images of CM (Kyse-30 cancer cell membrane), TPL/siHIF-1α@Zr-MOF, and TPL/siHIF-1α@Zr-MOF@CM. K) Flow cytometry detection of key cancer cell membrane markers (CD44, CD90, EGFR) on kyse-30 cells, kyse-30 cell membrane, and TPL/siHIF-1α@Zr-MOF@CM.

zeta potential changed to −11.7 mV (TPL/siHIF-1α@Zr-MOF@CM), which ensured the stable dispersion of the nanocomplex in the physiological environment (Fig. 1E). This is related to the negatively charged nature of the cell membrane and siRNA. UV–vis spectrum showed the characteristic absorption peak of free TPL at 220 nm was present in TPL@Zr-MOF@CM (Fig. 1F). Meanwhile, the fluorescence emission spectra of free siHIF-1α and TPL/siHIF-1α@Zr-MOF@CM showed strong fluorescence peaks at 524 nm (Fig. 1G). These results confirmed that TPL and siHIF-1α were successfully loaded into the nanomaterials. Notably, we also recorded the optical properties of the Zr-MOF nanomaterials and their organic ligand H_2TCPP by UV–Vis and fluorescence spectroscopy. In the UV–Vis absorption spectra, H_2TCPP showed an intense absorption band at 420 nm, while four weaker peaks within the 500–700 nm range (514, 549, 590, 650 nm), which corresponded to the B and Q bands of the porphyrin, respectively. The absorption peaks of the nanoparticles (Zr-MOF@CM and TPL@Zr-MOF@CM) were slightly lower than that of H_2TCPP, which may be due to the encapsulation effect of CM. Their fluorescence emission spectra showed that the nanoparticles (Zr-MOF@CM and TPL/siHIF-1α@Zr-MOF@CM) exhibited fluorescence intensities similar to those of the H_2TCPP solution (about 660 nm), demonstrating that the aggregation-induced quenching effect of H_2TCPP in the nanoparticles was relatively weak. These confirm that the prepared nanoparticles possess the characteristics of a photosensitizer.

FTIR further confirmed the structure of the nanoparticles. For Zr-MOF@CM, there was a C=O stretching peak at 1684 cm^{-1}, which was caused by the carboxylic acid; the characteristic peak in the 1612 cm^{-1} region was attributed to the O-C-O asymmetric stretching; the vicinity of 1506 and 1425 cm^{-1} showed the framework of the benzene ring. The peaks occurring in the TPL can be attributed to the specific functional groups, including the OH absorption peak at 3459.67 cm^{-1} and C=O absorption peak at 1772.26 cm^{-1}. Notably, the TPL@Zr-MOF@CM group displayed the same characteristic peaks as Zr-MOF@CM and TPL, which strongly confirmed the successful preparation of TPL@Zr-MOF@CM (Fig. 1H). In addition, XRD pattern detected a highly crystalline structure in Zr-MOF, while the diffraction peaks of TPL/siHIF-1α@Zr-MOF@CM remained consistent with it, indicating that CM and drug loading did not affect the crystal structure of Zr-MOF (Fig. 1I). The nitrogen adsorption-desorption isotherms of Zr-MOF, Zr-MOF@CM, and TPL/siHIF-1α@Zr-MOF@CM are shown in Fig. S1. According to the classification system of the International Union of Pure and Applied Chemistry, each material produced typical type I isotherm, indicating the presence of micropores in the materials. Notably, compared to the

other two materials, TPL/siHIF-1α had a lower adsorption, suggesting that the introduction of TPL and siHIF-1α occupied the internal channels and affected the surface area. SDS-PAGE results showed that TPL/siHIF-1α@Zr-MOF@CM and Kyse-30 CM had much similar electrophoretic phenotypes, indicating that the cloaking process did not affect the integrity and bioactivity of membrane proteins (Fig. 1J). Flow cytometry further revealed that TPL/siHIF-1α@Zr-MOF@CM had similar molecule expression (CD44, CD90, and EGFR) with Kyse-30 cells or membranes (Fig. 1K). These findings confirm the successful preparation of bionic membranes.

Following, we observed that the particle size and particle size distribution of TPL/siHIF-1α@Zr-MOF@CM did not change significantly with the extension of time under PBS or 10 % FBS environment, indicating that the prepared nanoparticles were stable in both aqueous and physiological conditions (Fig. 2A and B). The drug loading rate evaluation revealed that the drug loading rates of TPL and siHIF-1α in TPL/siHIF-1α@Zr-MOF@CM were 20.56 % and 22.59 %, respectively (Fig. 2C and D). In addition, compared to the neutral pH7.4 (simulated normal environment), TPL/siHIF-1α@Zr-MOF@CM significantly enhanced the cumulative release of TPL and siHIF-1α in acidic pH5.5 (simulated tumor microenvironment) and reached ~70 % release at 36 h, indicating that the nanoparticles had pH-sensitive properties (Fig. 2E and F). Under 660 nm irradiation stimulation, it was found that both Zr-MOF and TPL/siHIF-1α@Zr-MOF@CM could produce $^1O_2$ at 410 nm (Fig. 2G). Moreover, we found that the peak at 455 nm in the UV–Vis spectrum of TPL/siHIF-1α@Zr-MOF@CM increased with time under 660 nm laser irradiation, indirectly indicating the formation of •OH (Fig. S2). This discovery confirmed the potential of prepared nanoparticles for application in PDT.

3.2. The biocompatibility of TPL/siHIF-1α@Zr-MOF@CM in vitro

As a prerequisite for the clinical development, we explored the biocompatibility of TPL/siHIF-1α@Zr-MOF@CM in vitro. The

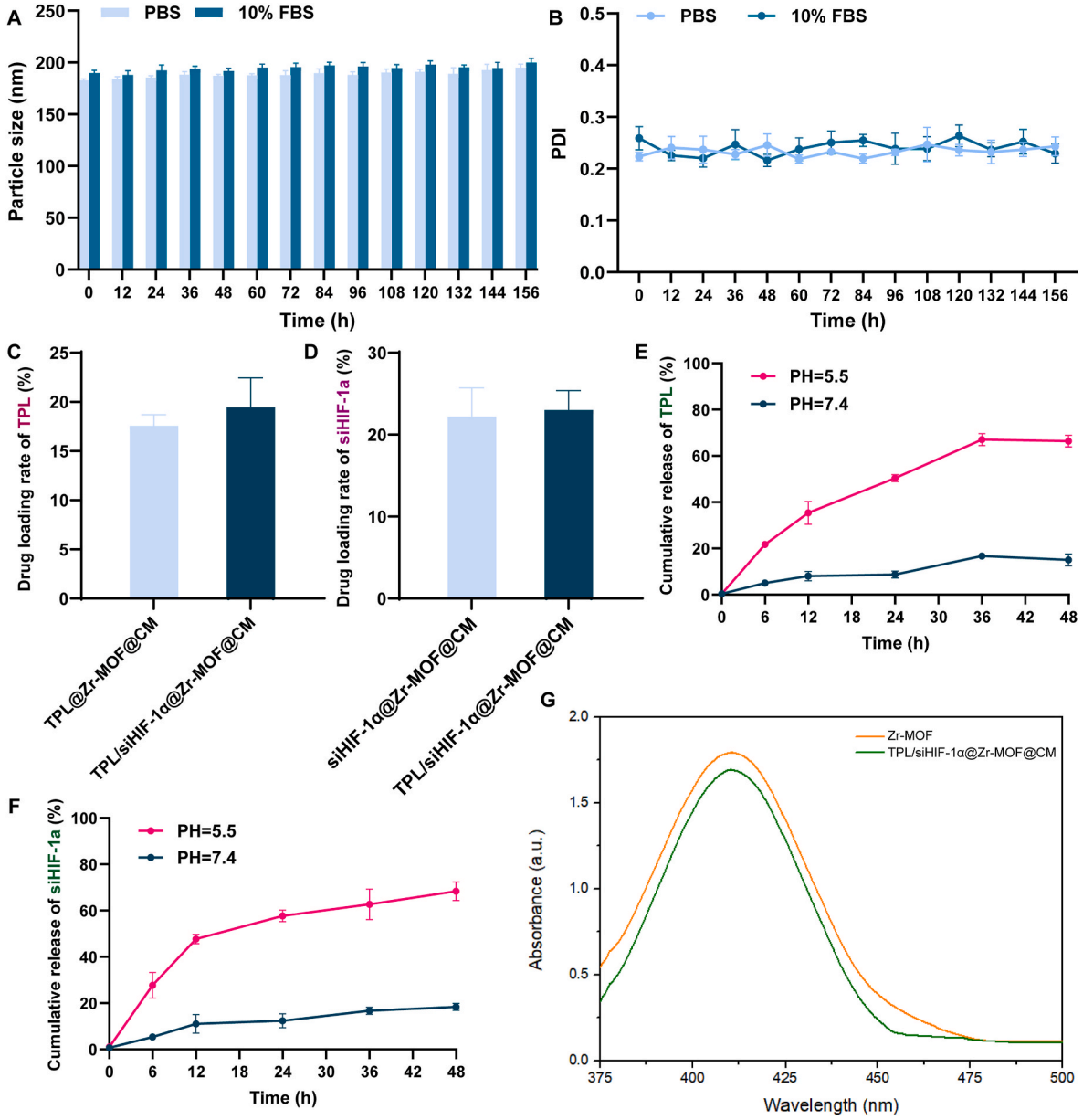

Fig. 2. Stability and pH sensitivity analysis of TPL/siHIF-1α@Zr-MOF@CM. A and B) Size stability of TPL/siHIF-1α@Zr-MOF@CM in PBS or 10 % FBS environments. C and D) Drug loading rate of TPL and siHIF-1α. E and F) Cumulative release curves of TPL and siHIF-1α from TPL/siHIF-1α@Zr-MOF@CM at different pHs of 5.5 and 7.4. G) Detection of $^1O_2$ production from TPL/siHIF-1α@Zr-MOF@CM under 660 nm laser by UV–visible spectroscopy.

cytotoxicity assessment indicated that the toxicity of Zr-MOF and Zr-MOF@CM to Kyse-30 or HEEC cells was negligible (Fig. 3A and B). The hemolysis test showed that even with the addition of high concentration of TPL/siHIF-1α@Zr-MOF@CM (200 μg/mL), no obvious hemolysis of erythrocytes occurred, and the hemolysis rate was less than 2 %, which verified the good blood compatibility of TPL/siHIF-1α@Zr-MOF@CM (Fig. 3C). Besides, TPL/siHIF-1α@Zr-MOF@CM exhibited dose-dependent cytotoxicity to cancer cells with an IC_{50} value of 50 μg/mL (Fig. 3D). It is known that effective uptake of nanoparticles within cancer cells is critical for their therapeutic efficacy. In addition, cancer cell membrane camouflaged nanoparticles demonstrate homologous targeting specificity, further enhancing the effectiveness of the therapeutic drugs. Hence, we verified the targeting ability of TPL/siHIF-1α@Zr-MOF@CM on Kyse-30 cells through flow cytometry and CLSM, using TPL/siHIF-1α@Zr-MOF as a control (Fig. 3E and F). CLSM showed that Kyse-30 cells treated with TPL/siHIF-1α@Zr-MOF@CM exhibited stronger red fluorescence than TPL/siHIF-1α@Zr-MOF. The red fluorescence was enhanced with the extension of co-incubation time and most of the red signals were observed to be localized in the cytoplasm. Meanwhile, flow cytometry quantitative analysis further confirmed this phenomenon. After incubating Kyse-30 cells with nanoparticles, especially TPL/siHIF-1α@Zr-MOF@CM, the fluorescence intensity was significantly increased. These results suggested that cancer cell membrane camouflage promoted the uptake of nanoparticles within cells. In addition, cell activity was significantly suppressed with increasing power (Fig. 3G). Next, we analyzed the ability of nanoparticles to promote ROS production in the cells using DCF-DA staining. Under laser irradiation, Kyse-30 cells treated with Zr-MOF@CM or TPL/siHIF-1α@Zr-MOF@CM showed strong green fluorescence, suggesting the intracellular production of ROS. Meanwhile, quantitative analysis showed that the fluorescence intensity was highest in the TPL/siHIF-1α@Zr-MOF@CM + Laser treatment group, which once again confirmed the generation of ROS (Fig. 3H). This is because after TPL/siHIF-1α@Zr-MOF@CM is internalized by cancer cells, the released TPL and siHIF-1α further stimulate the ROS production. These results further suggested that TPL/siHIF-1α@Zr-MOF@CM can be effectively internalized by Kyse-30 cells and also produce excess ROS under the stimulation of visible light to cause oxidative damage to cells.

3.3. The anti-tumor efficacy of TPL/siHIF-1α@Zr-MOF@CM in vitro

The above findings confirmed that TPL/siHIF-1α@Zr-MOF@CM can accelerate the drug release behavior after laser irradiation, thus facilitating the combination therapy of esophageal cancer. Afterwards, we explored the therapeutic effects of nanoparticles combined with laser irradiation on Kyse-30 cells. The synergistic cytotoxicity of different treatments in cells was first evaluated by CCK-8 experiments (Fig. 4A). It was found that the nanomaterial Zr-MOF@CM exhibited negligible cytotoxicity in the absence of laser irradiation. However, the addition of 660 nm laser increased the inhibitory effect of Zr-MOF@CM on cell viability. In addition, the viability of Kyse-30 cells was obviously decreased after the treatment of nanocomplexes including TPL@Zr-MOF@CM, siHIF-1α@Zr-MOF@CM, and TPL/siHIF-1α@Zr-MOF@CM, suggesting that the nanoparticle-released TPL and/or siHIF-1α had a certain killing effect on cancer cells. As expected, the cytotoxic effect of the combination groups (nanocomplex + laser) increased significantly and was remarkably higher than those of the corresponding treatment group alone. In particular, TPL/siHIF-1α@Zr-MOF@CM + laser had the strongest cell inhibition effect. We also detected the apoptosis level of all groups by flow cytometry. The results revealed that kyse-30 cells treated with TPL/siHIF-1α@Zr-MOF@CM + laser showed obvious apoptosis, with much higher number of apoptotic cells than other groups (Fig. 4B and D). Besides, live/dead cell staining images indicated that cells incubated with the nanocomplex alone for 24 h caused a few cell deaths (red fluorescence) due to the cytotoxic effect of the released drug. After laser irradiation, the number of dead cancer cells dramatically increased

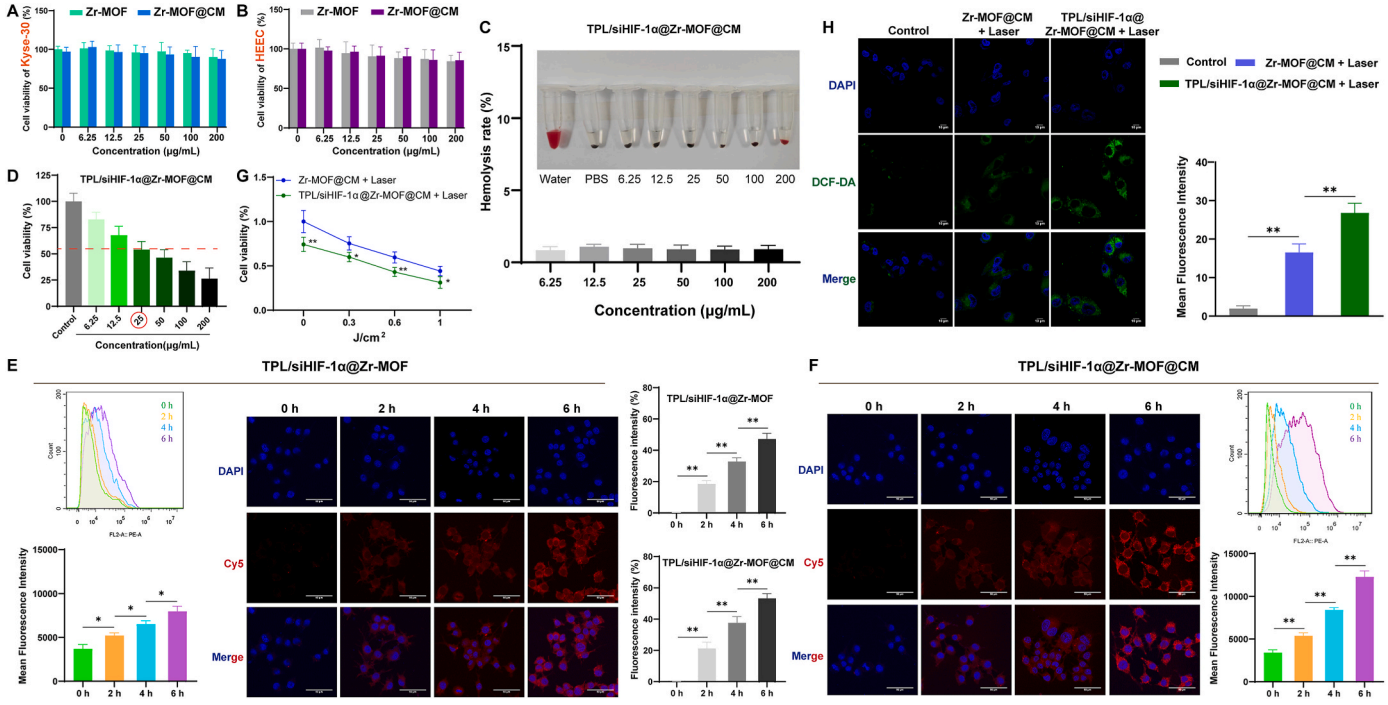

Fig. 3. Cytotoxicity, cellular uptake, and ROS generation capacities of TPL/siHIF-1α@Zr-MOF@CM. A and B) Cytotoxicity of nanomaterials (Zr-MOF and Zr-MOF@CM) in Kyse-30 and HEEC cells assessed by CCK-8. C) Hemolysis rates at varying concentrations of TPL/siHIF-1α@Zr-MOF@CM from 6.25, 12.5, 25, 50, 100, 200 μg/mL. D) Toxicity of TPL/siHIF-1α@Zr-MOF@CM to Kyse-30 cells. E and F) Cellular uptake of TPL/siHIF-1α@Zr-MOF or TPL/siHIF-1α@Zr-MOF@CM after 2, 4, and 6 h of incubation with Kyse-30 cells by flow cytometry and CLSM images (scale bar, 50 μm). G) Cell viability of Kyse-30 cells treated with Zr-MOF@CM or TPL/siHIF-1α@Zr-MOF@CM under different doses of 660 nm laser irradiation. H) Fluorescence images (scale bar, 10 μm) and statistical quantification of ROS production in Kyse-30 cells treated with Zr-MOF@CM and TPL/siHIF-1α@Zr-MOF@CM under 660 nm laser irradiation. **P < 0.01.

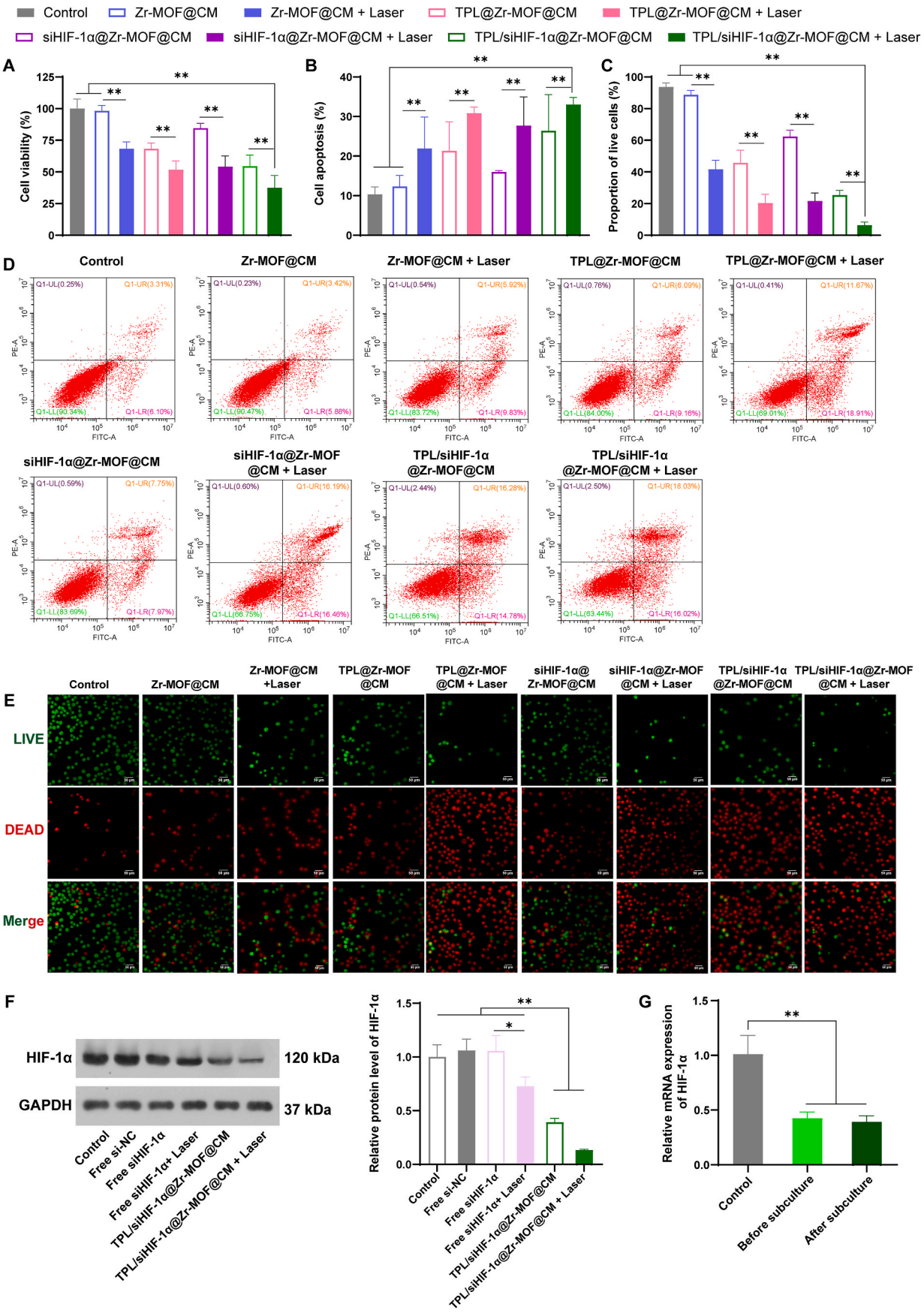

(caption on next page)

Fig. 4. In vitro antitumor efficiency of TPL/siHIF-1α@Zr-MOF@CM in esophageal cancer cells. A) Cell viability of Kyse-30 cells incubated with Zr-MOF@CM, TPL@Zr-MOF@CM, siHIF-1α@Zr-MOF@CM, and TPL/siHIF-1α@Zr-MOF@CM for 24 h with or without 660 nm laser irradiation. B) The quantified apoptosis levels in different treatment groups. C) The proportion of live cells in different treatment groups. D) Apoptosis levels of Kyse-30 cells in different treatment groups detected by flow cytometry. E) Images of Kyse-30 cells stained with calcein AM (green, live cells) and propidium iodide (red, dead cells) after co-incubation with different nanoparticles for 24 h with or without 660 nm laser irradiation (scale bar, 50 μm). F) Protein expression of HIF-1α in control, free si-NC, free siHIF-1α, free siHIF-1α + laser, TPL/siHIF-1α@Zr-MOF@CM, and TPL/siHIF-1α@Zr-MOF@CM + laser groups tested via western blot. (G) qRT-PCR detection of HIF-1α expression levels in TPL/siHIF-1α@Zr-MOF@CM-treated Kyse-30 cells before and after subculture. $^{**}P < 0.01$. (For interpretation of the references to color in this figure legend, the reader is referred to the Web version of this article.)

compared to the nanoparticle-treated group alone, especially the TPL/siHIF-1α@Zr-MOF@CM + laser group presented bright red fluorescence, with almost all of the cancer cells dying (Fig. 4C and E). Further qRT-PCR and western blot analysis confirmed that TPL/siHIF-1α@Zr-MOF@CM could stably knock down HIF-1α and laser treatment further suppressed HIF-1α expression (Figure S3 and Fig. 4F). Because free siRNAs are hydrophilic and carry a large amount of negative charge, this makes it difficult for them to enter the cell membrane by passive diffusion, leading to an insufficient effective intracellular concentration of them to significantly inhibit HIF-1α expression. Of interest, after successive passaging cultures (three generations), qRT-PCR analysis verified that TPL/siHIF-1α@Zr-MOF@CM still maintained stable ability to knock out HIF-1α (Fig. 4G). Taken together, TPL/siHIF-1α@Zr-MOF@CM showed satisfactory anticancer effects under laser irradiation, which may be attributed to its mediated photodynamic effect.

3.4. Synergistic photodynamic/drug/gene therapy of TPL/siHIF-1α@Zr-MOF@CM in vivo

The ultimate goal of this study was to confirm the therapeutic efficacy and biosafety of TPL/siHIF-1α@Zr-MOF@CM in BALB/c mice carrying Kyse-30 (esophageal squamous cells) xenograft tumors (Fig. 5A). For this purpose, we inoculated Kyse-30 cells into BALB/c mice and then elevated in vivo biodistribution as well as tumor targeting ability of nanoparticles by intravenous injection of Cy5-labeled nanoparticles (TPL/siHIF-1α@Zr-MOF or TPL/siHIF-1α@Zr-MOF@CM). As shown in Fig. 5B, in vivo imaging analysis showed that the fluorescence signal of TPL/siHIF-1α@Zr-MOF at the tumor site gradually increased with the injection time, and reached the maximum accumulation at 6 h. Notably, cell membrane encapsulation further increased the accumulation/residence time of nanoparticles in the tumor, and the fluorescence signal was still observed 48 h after injection. In contrast, the fluorescence signals at the tumor site of mice injected with TPL/siHIF-1α@Zr-MOF were relatively weak and gradually disappeared after 8 h of injection. Mice were euthanized 48 h after injection. Ex vivo image of major organs indicated that the fluorescent signals of nanoparticles were mainly distributed in tumors and cell membrane-encapsulated TPL/siHIF-1α@Zr-MOF displayed higher tumor accumulation. Besides, the liver and kidney also showed clear fluorescence signals, which may be due to drug metabolism (Fig. 5C).

Following, we evaluated the therapeutic effects of the different treatment protocols (nanoparticles or nanoparticles combined with laser) in tumor-bearing mice. During the treatment period, there was no significant fluctuation in the body weight of the mice from all groups, indicating that the nanoparticles had excellent biosafety (Fig. 5D). At the early stage of treatment, TPL/siHIF-1α@Zr-MOF@CM exhibited a certain inhibitory effect on tumor growth. However, the tumor volume of mice in this group showed an increasing trend after 10 days, indicating that the tumor inhibitory effect of TPL/siHIF-1α@Zr-MOF@CM treatment was limited. Strikingly, 660 nm laser irradiation enhanced the antitumor effects of nanoparticles, especially the combination of TPL/siHIF-1α@Zr-MOF@CM and laser continued to show excellent tumor suppression in the later stages of treatment (Fig. 5E). This finding was further confirmed in the photographs of the resected tumors in each group (Fig. 5F and Fig. S4). This may be due to the fact that laser irradiation can stimulate the photosensitizer Zr-MOF to produce excessive ROS, which reacts with biomolecules in tumor cells and thus enhances the anti-tumor effect of nanoparticles [35]. In addition, TUNEL and Ki67 staining were applied for pathological detection of mouse tumors. As shown in Fig. 5G, a large number of apoptotic cancer cells (green fluorescence) were observed in the TPL/siHIF-1α@Zr-MOF@CM treated mice under laser irradiation, whereas the other groups displayed relatively little green fluorescence, demonstrating that this treatment maximally induced apoptosis and necrosis in tumor tissues. We also observed that the Ki67 protein levels were lowest in the TPL/siHIF-1α@Zr-MOF@CM + Laser group compared to the other three groups, confirming that the proliferation activity of tumor cells was clearly suppressed (Fig. 5H). Moreover, western blot analysis revealed that TPL/siHIF-1α@Zr-MOF@CM effectively down-regulated the HIF-1α level in mouse tumor tissues, and the addition of laser further increased this inhibitory effect (Fig. 5I). Surprisingly, HE analysis of slices of major mouse organs showed no significant pathological changes in the heart, liver, spleen, lung, and kidneys in all treatment groups, confirming the safety of nanoparticles/combination therapy and the biocompatibility of the selective action on tumor sites (Fig. 6). Overall, these findings provide compelling evidence that the developed TPL/siHIF-1α@Zr-MOF@CM had strong tumor targeting ability and can exert better anti-tumor effect by combination with laser.

4. Discussion

Based on the available evidences, nanoparticles provide a number of potential advantages over the conventional formulations in cancer therapy, such as preventing premature drug degradation, enhancing drug uptake in the specific tumor tissues, and finally improving the effectiveness of treatment. With the increasing demand for more effective and safer therapeutic strategies, stimulus-responsive nano-delivery systems have attracted a lot of attention, especially in oncology [36–38]. For example, PDT-based nanosystems allow for the formation of cytotoxic ROS through the use of photosensitizers and light, and the subsequent aggregation of the treatment to light-irradiated tissues. As a result, there has been significant focus on the application of nanoplatforms for PDT in cancer [39–41]. This approach offers excellent temporal and spatial controllability, low invasiveness and less drug tolerance. However, the hypoxic condition of solid tumors significantly limits the efficacy of PDT, as the low oxygen levels prevent the generation of ROS, which cannot be produced at a rate sufficient to achieve a significant therapeutic effect. In order to address the issues in PDT, the application of nanoparticles has been suggested [42]. Hence, exploring effective methods to alleviate hypoxia has become extremely important in the clinical application of PDT. Based on this concept, we prepared biomimetic TPL/siHIF-1α@Zr-MOF@CM nanoparticles for the combined treatment of esophageal cancer.

In this study, we selected the chemically stable Zr-MOF as the photosensitive nano-transfer system and confirmed its excellent performance through a series of experiments. Firstly, the nanomaterial Zr-MOFs possess high photosensitizer loading and good biocompatibility, which can maintain long-term stability under physiological environment. Secondly, the uniform distribution and porous structure of Zr-MOF provide the loading drug with high efficiency. Results showed that the drug loading rate of TPL reached about 20 % and effectively suppressed the expression of HIF-1α. Thirdly, to avoid the nanoparticles from being captured and cleared by the immune system, we utilized homologous cancer cell membrane as the coat of Zr-MOF and confirmed

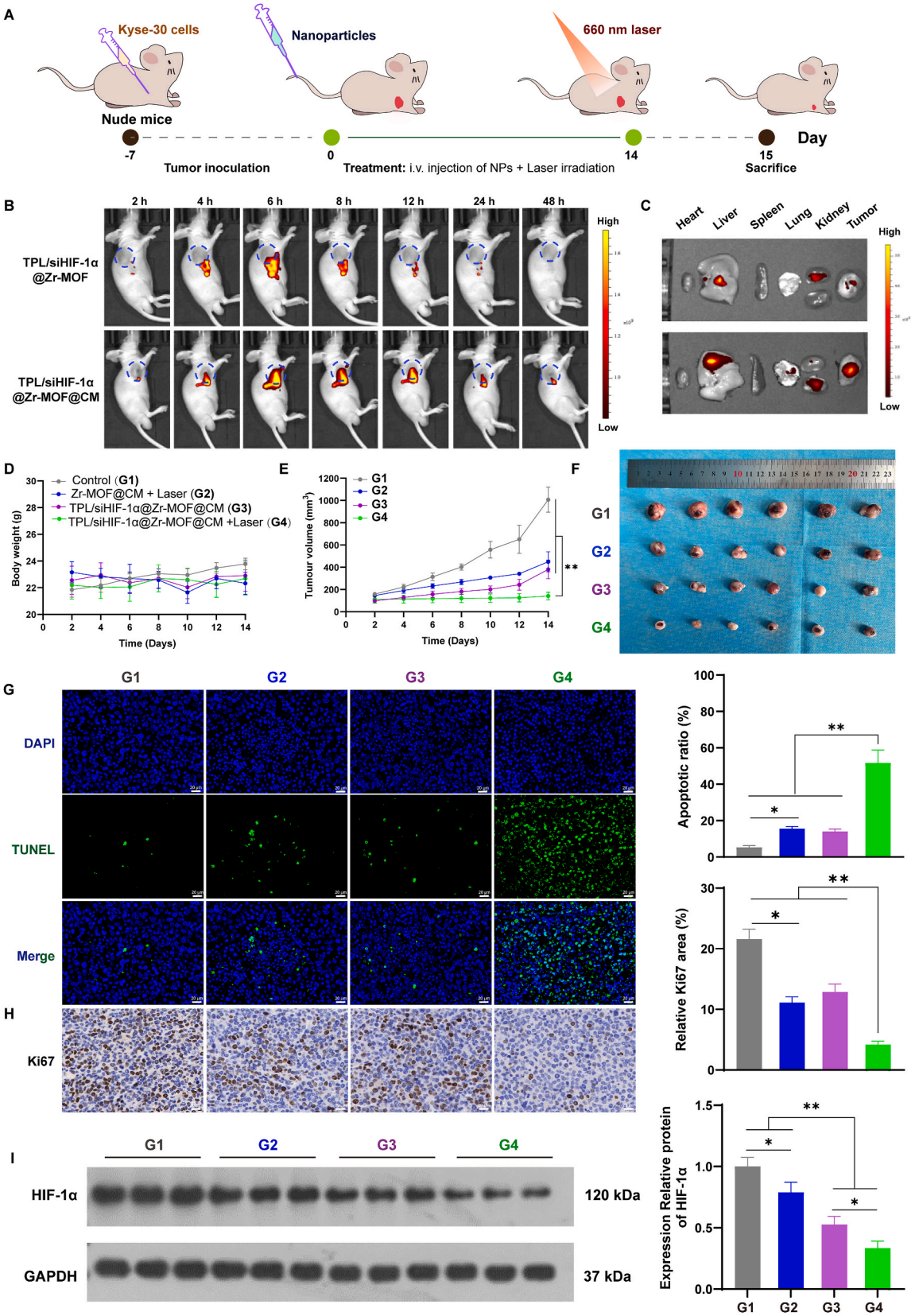

Fig. 5. In vivo distribution and antitumor effects of TPL/siHIF-1α@Zr-MOF@CM in Kyse-30 tumor-bearing mouse model. A) Scheme illustration the construction and treatment of Kyse-30 tumor-bearing mouse model. B) Fluorescence images of tumor-bearing mice at 2, 4, 6, 8, 12, 24, and 48 h after intravenous injection of TPL/siHIF-1α@Zr-MOF and TPL/siHIF-1α@Zr-MOF@CM. C) Ex vivo distribution of TPL/siHIF-1α@Zr-MOF and TPL/siHIF-1α@Zr-MOF@CM in major organs at 48 h. D and E) Body weight and tumor volume changes within 14 days of mice from control, Zr-MOF@CM + laser, TPL/siHIF-1α@Zr-MOF@CM, and TPL/siHIF-1α@Zr-MOF@CM + laser groups. F) Representative photographs of dissected tumors. G and H) TUNEL staining and Ki67 immunohistochemical analysis of tumor tissue slices (scale bar, 20 μm). I) Expression level of HIF-1α in tumor tissue from different groups. *P < 0.05, **P < 0.01.

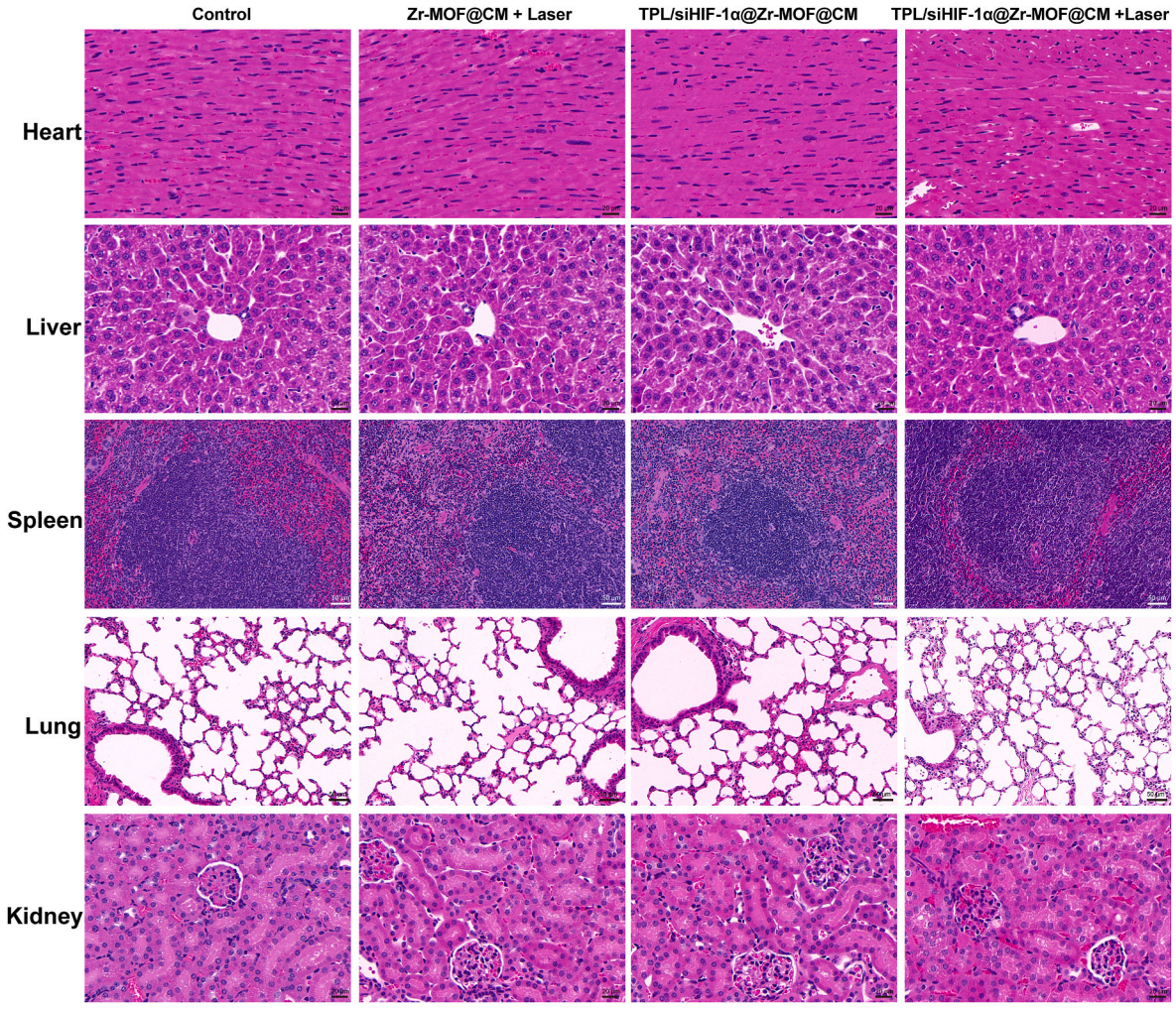

Fig. 6. H&E staining of vital organs (heart, liver, spleen, lung, and kidney) to assess the safety of nanoparticles in vivo.

the retention of cancer cell membrane-specific molecules on Zr-MOF@CM by flow cytometry and SDS-PAGE, demonstrating that esophageal cancer cell membranes were successfully coated on the TPL/siHIF-1α@Zr-MOF nanoparticles. This cancer cell membrane encapsulation technique gives the stealth function of nanoparticles, which not only extends the time of the drugs in the bloodstream, but also retains homologous recognition and homing properties. Finally, we also observed that under 660 nm laser irradiation, TPL/siHIF-1α@Zr-MOF@CM produced a large amount of toxic •OH and $^1O_2$, and then catalyzed the generation of intracellular ROS in tumor cells, resulting in oxidative stress and cytotoxicity. Meanwhile, the porous nature of Zr-MOF makes it easy for ROS to diffuse and may have a higher PDT effect than other nanoparticles. These findings confirm that this nanoscale drug carrier have better physicochemical properties and exert great potential for biological application.

Following, we focused on evaluating the anti-tumor effects and biosafety of the nanomedicines in vitro and in vivo. The results revealed that TPL/siHIF-1α@Zr-MOF@CM had pH-dependent drug release behavior. Meanwhile, flow cytometry and CLSM showed that CM coating and longer incubation time significantly increased the uptake rate of nanoparticles by Kyse-30 cells. The pH sensitivity and effective uptake within cancer cells are the foundation for their therapeutic effects. In the blood circulatory system (pH 7.4), the stability of nanoparticles protects the integrity of the drug/siRNA biological structure and prevents drug dissociation/release. Once exposed to the acidic environment of tumor tissues (pH 5.5), the nanoparticles exhibit specific recognition of tumor cells and are effectively internalized by cells; further, the nanoparticles disintegrated and successfully released the drug/siRNA into the cytoplasm. In vitro functional experiments indicated that TPL/siHIF-1α@Zr-MOF@CM could effectively inhibit the viability of Kyse-30 cells and percentage of live cells, while promoting the proportion of apoptotic cells. As expected, 660 nm laser irradiation significantly enhanced the anti-cancer effect of TPL/siHIF-1α@Zr-MOF@CM. This reaffirms that photoinduced ROS production induces PDT synergistic drugs showing effective tumor killing effects. Afterwards, we monitored the biological distribution and targeting behavior of these nanoparticles in vivo. In the tumor-bearing mice, the fluorescence signals of nanomedicines at the tumor site were gradually enhanced with the extension of the injection time, and reached a peak at 6 h. Obviously, the presence of cancer cell membranes further increased the retention and accumulation of nanoparticles in tumors, which was attributed to the homologous targeting ability of cancer cell membranes [32]. These results strongly confirmed that TPL/siHIF-1α@Zr-MOF@CM had excellent tumor targeting ability. In vivo antitumor analysis indicated that TPL/siHIF-1α@Zr-MOF@CM down-regulated the expression of the proliferation markers (Ki67 and HIF-1α) under 660 nm radiation exposure, and exhibited overwhelming tumor suppression efficiency. In order to maximize the treatment of cancer, the combination therapy has been suggested [43,44]. Of interest, nanoparticle administration did not significantly affect the body weight of tumor bearing mice and did not cause obvious tissue damage to major organs, suggesting that the developed TPL/siHIF-1α@Zr-MOF@CM had a favorable biosafety

profile.

To the best of our knowledge, this work is the first successful construction of a nanoplatform for targeted co-delivery of TPL/siHIF-1α, and this delivery system realizes the synergistic effect of highly effective drug-PDT, which provides new perspectives for expanding the application of nanomedicines. However, there are several pressing issues to be solved before clinical transformation. For example, the pharmacokinetics and long-term efficacy/safety of nanoparticles have not been observed. In addition, this study used a subcutaneous tumor xenograft model, which could not simulate the complex microenvironment and metastasis of primary cancer. Moreover, future studies are encouraged to focus on the surface modification of these nanoplatforms with membranes obtained from other cells such as macrophages and platelets, among others to compare the efficacy. Another important aspect can be the evaluation of immunotherapeutic feature of these nanoplatforms or their combination with immune checkpoint inhibitors to suppress esophageal cancer and this area can be explored in the future. Since these nanoparticles can affect the TME, it is suggested that future studies focus on the TME remodeling feature of these nanoplatforms.

5. Conclusion

In this study, TPL and siHIF-1α were encapsulated simultaneously into Zr-MOF nanomaterials, and then the nanoparticles were coated by tumor cell membranes with homologous targeting ability, successfully constructing a biomimetic nanomedicine (TPL/SIHIF-1α@Zr-MOF@CM). The nanomaterials remained stable under physiological conditions and had good biosafety in vitro and in vivo. We noted that the functionalized nanoparticles had high drug loading rate and can be effectively absorbed by Kyse-30 cells. Meanwhile, the photosensitizer in the nanoparticles generated ROS under laser irradiation, thereby killing tumor cells. TPL and HIF-1α inhibition further amplified the oxidative damage in the tumor site. In vivo, the intrinsic properties of cancer cell membranes prolonged the circulation time of the nanoparticles in body and facilitated their selective cancer cell-targeting ability, ensuring effective drug delivery. Of interest, TPL/siHIF-1α@Zr-MOF@CM exhibited satisfactory inhibition of tumor growth and enhanced antitumor efficacy through the synergistic effect of PDT-chemotherapy. Collectively, this convenient delivery system provides a comprehensive treatment option for esophageal cancer and may have broad application prospects in the complementary therapies for malignant tumors.

CRediT authorship contribution statement

Wenhan Liu: Writing – review & editing, Investigation, Writing – original draft. **Can Sun:** Writing – original draft, Writing – review & editing, Investigation. **Yuhang Dai:** Writing – review & editing, Investigation, Writing – original draft. **Huaiyong Wang:** Writing – original draft, Writing – review & editing, Investigation. **Milad Ashrafizadeh:** Writing – original draft, Investigation, Conceptualization, Writing – review & editing, Validation. **João Conde:** Writing – review & editing, Validation, Conceptualization, Writing – original draft, Data curation. **Liyu Yang:** Writing – original draft, Supervision, Data curation, Writing – review & editing, Validation, Funding acquisition, Conceptualization. **Wei He:** Writing – review & editing, Validation, Funding acquisition, Conceptualization, Writing – original draft, Supervision, Data curation.

Declaration of competing interest

J.C. is a co-founder and shareholder of TargTex S.A. – Targeted therapeutics for Glioblastoma Multiforme. J.C. is also a member of the Global Burden Disease (GBD) consortium of the Institute for Health Metrics and Evaluation (IHME), University of Washington (US). All other authors declare no conflicts of interest.

Appendix A. Supplementary data

Supplementary data to this article can be found online at https://doi.org/10.1016/j.mtbio.2025.102183.

Data availability

Data will be made available on request.

References

[1] H. Sung, et al., Global cancer statistics 2020: GLOBOCAN estimates of incidence and mortality worldwide for 36 cancers in 185 countries, CA Cancer J. Clin. 71 (3) (2021) 209–249.
[2] E. Morgan, et al., The global landscape of esophageal squamous cell carcinoma and esophageal adenocarcinoma incidence and mortality in 2020 and projections to 2040: new estimates from GLOBOCAN 2020, Gastroenterology 163 (3) (2022) 649–658.e2.
[3] N. Deboever, et al., Advances in diagnosis and management of cancer of the esophagus, BMJ (Clinical Research ed.) 385 (2024) e074962.
[4] C.T. Demarest, A.C. Chang, The landmark series: multimodal therapy for esophageal cancer, Ann. Surg Oncol. 28 (6) (2021) 3375–3382.
[5] Q.-L. Xu, et al., The treatments and postoperative complications of esophageal cancer: a review, J. Cardiothorac. Surg. 15 (1) (2020) 163.
[6] T. Simon-Yarza, et al., Nanoparticles of metal-organic frameworks: on the road to in vivo efficacy in biomedicine, Advanced Materials (Deerfield Beach, Fla.) 30 (37) (2018) e1707365.
[7] S. Huang, et al., Current and promising applications of MOFs loaded with PTAs on photothermal therapy, React. Funct. Polym. 193 (2023) 105743.
[8] Q. Huang, et al., Metal-organic framework-based dressings: application and opportunities in wound healing, Mater. Today Chem. 40 (2024) 102235.
[9] M. Guo, et al., Prospective feasibilities and strategies of MOFs on the treatment of oropharyngeal carcinoma, Mater. Today Chem. 45 (2025) 102627.
[10] M.X. Wu, Y.W. Yang, Metal–organic framework (MOF)-based drug/cargo delivery and cancer therapy, Adv. Mater. 29 (23) (2017) 1606134.
[11] Z.-X. Chen, et al., Interfering with lactate-fueled respiration for enhanced photodynamic tumor therapy by a porphyrinic MOF nanoplatform, Adv. Funct. Mater. 28 (36) (2018) 1803498.
[12] X. Chen, et al., A fluorinated BODIPY-based zirconium metal–organic framework for in vivo enhanced photodynamic therapy, J. Am. Chem. Soc. 146 (2) (2024) 1644–1656.
[13] M. Kolarikova, et al., Photodynamic therapy: innovative approaches for antibacterial and anticancer treatments, Med. Res. Rev. 43 (4) (2023) 717–774.
[14] X. Li, et al., Clinical development and potential of photothermal and photodynamic therapies for cancer, Nat. Rev. Clin. Oncol. 17 (11) (2020) 657–674.
[15] A.P. Castano, P. Mroz, M.R. Hamblin, Photodynamic therapy and anti-tumour immunity, Nat. Rev. Cancer 6 (7) (2006) 535–545.
[16] S.B. Brown, E.A. Brown, I. Walker, The present and future role of photodynamic therapy in cancer treatment, Lancet Oncol. 5 (8) (2004) 497–508.
[17] Z. Chen, et al., Hypoxic microenvironment in cancer: molecular mechanisms and therapeutic interventions, Signal Transduct. Targeted Ther. 8 (1) (2023) 70.
[18] L. Larue, et al., Fighting hypoxia to improve PDT, Pharmaceuticals 12 (4) (2019) 163.
[19] J. Dang, et al., Manipulating tumor hypoxia toward enhanced photodynamic therapy (PDT), Biomater. Sci. 5 (8) (2017) 1500–1511.
[20] M.E. Rodríguez, et al., A novel HIF-1α/VMP1-autophagic pathway induces resistance to photodynamic therapy in Colon cancer cells, Photochem. Photobiol. Sci. : Official Journal of the European Photochemistry Association and the European Society For Photobiology 16 (11) (2017) 1631–1642.
[21] Y. Sun, et al., Recent progress of hypoxia-modulated multifunctional nanomedicines to enhance photodynamic therapy: opportunities, challenges, and future development, Acta Pharm. Sin. B 10 (8) (2020) 1382–1396.
[22] P. Liu, et al., Oxygen-self-supplying and HIF-1α-Inhibiting core-shell nanosystem for hypoxia-resistant photodynamic therapy, ACS Appl. Mater. Interfaces 11 (51) (2019) 48261–48270.
[23] G. Kara, G.A. Calin, B. Ozpolat, RNAi-based therapeutics and tumor targeted delivery in cancer, Adv. Drug Deliv. Rev. 182 (2022) 114113.
[24] Y.-K. Oh, T.G. Park, siRNA delivery systems for cancer treatment, Adv. Drug Deliv. Rev. 61 (10) (2009) 850–862.
[25] H.J. Kim, et al., Recent progress in development of siRNA delivery vehicles for cancer therapy, Adv. Drug Deliv. Rev. 104 (2016) 61–77.
[26] Y. Wang, et al., Construct of MoSe2/Bi2Se3 nanoheterostructure: multimodal CT/PT imaging-guided PTT/PDT/chemotherapy for cancer treating, Biomaterials 217 (2019) 119282.
[27] H. Lee, et al., Combination of chemotherapy and photodynamic therapy for cancer treatment with sonoporation effects, J. Contr. Release 283 (2018) 190–199.
[28] G. Canti, et al., Antitumor efficacy of the combination of photodynamic therapy and chemotherapy in murine tumors, Cancer Lett. 125 (1) (1998) 39–44.
[29] B. Xu, et al., Triptolide simultaneously induces reactive oxygen species, inhibits NF-κB activity and sensitizes 5-fluorouracil in colorectal cancer cell lines, Cancer Lett. 291 (2) (2010) 200–208.

[30] J. Yang, et al., Expanded ROS generation and hypoxia reversal: excipient-free self-assembled nanotheranostics for enhanced cancer photodynamic immunotherapy, Advanced Materials (Deerfield Beach, Fla.) 36 (30) (2024) e2402720.
[31] R.H. Fang, et al., Cell membrane coating nanotechnology, Advanced Materials (Deerfield Beach, Fla.) 30 (23) (2018) e1706759.
[32] R.H. Fang, W. Gao, L. Zhang, Targeting drugs to tumours using cell membrane-coated nanoparticles, Nat. Rev. Clin. Oncol. 20 (1) (2023) 33–48.
[33] W. Song, et al., Cell membrane-camouflaged inorganic nanoparticles for cancer therapy, J. Nanobiotechnol. 20 (1) (2022) 289.
[34] H. Min, et al., Biomimetic metal-organic framework nanoparticles for cooperative combination of antiangiogenesis and photodynamic therapy for enhanced efficacy, Advanced Materials (Deerfield Beach, Fla.) 31 (15) (2019) e1808200.
[35] D. Gao, et al., Modified nanoscale metal organic framework-based nanoplatforms in photodynamic therapy and further applications, Photodiagnosis Photodyn. Ther. 32 (2020) 102026.
[36] S. Mura, J. Nicolas, P. Couvreur, Stimuli-responsive nanocarriers for drug delivery, Nat. Mater. 12 (11) (2013) 991–1003.
[37] X. Zhao, et al., Dual-stimuli responsive and reversibly activatable theranostic nanoprobe for precision tumor-targeting and fluorescence-guided photothermal therapy, Nat. Commun. 8 (1) (2017) 14998.
[38] J. Noh, et al., Amplification of oxidative stress by a dual stimuli-responsive hybrid drug enhances cancer cell death, Nat. Commun. 6 (1) (2015) 6907.
[39] N.M. Idris, et al., In vivo photodynamic therapy using upconversion nanoparticles as remote-controlled nanotransducers, Nat. Med. 18 (10) (2012) 1580–1585.
[40] Y. Cheng, et al., Perfluorocarbon nanoparticles enhance reactive oxygen levels and tumour growth inhibition in photodynamic therapy, Nat. Commun. 6 (1) (2015) 8785.
[41] Y. Zhang, et al., Harnessing copper-palladium alloy tetrapod nanoparticle-induced pro-survival autophagy for optimized photothermal therapy of drug-resistant cancer, Nat. Commun. 9 (1) (2018) 4236.
[42] I.R. Calori, H. Bi, A.C. Tedesco, Expanding the limits of photodynamic therapy: the design of organelles and hypoxia-targeting nanomaterials for enhanced photokilling of cancer, ACS Appl. Bio Mater. 4 (1) (2021) 195–228.
[43] N. Zheng, et al., Cationic polyporphyrins as siRNA delivery vectors for photodynamic and gene synergistic anticancer therapy, ACS Appl. Mater. Interfaces 13 (23) (2021) 27513–27521.
[44] Y. Jiang, et al., siRNA-Based carrier-free system for synergistic chemo/chemodynamic/RNAi therapy of drug-resistant tumors, ACS Appl. Mater. Interfaces 14 (1) (2022) 361–372.